

DFT and molecular docking study of a benzastatin alkaloids: Reactivity, cyclization mechanism, and antimalarial potential against plasmodium falciparum

Kenzy Charles^{a,b}, Zeroual Abdellah^{a*}, Mohammed Salah^a and Hocine Garmes^b

^aMolecular Modeling and Spectroscopy Research Team, Department of Chemistry, Faculty of Sciences, Chouaib Doukkali University, El Jadida, Morocco

^bAnalytical Chemistry and Environmental Sciences Team, Department of Chemistry, Water and Environment Laboratory, Faculty of Sciences of El Jadida. Chouaib Doukkali University, B. P. 20, 24000 El Jadida, Morocco

CHRONICLE

Article history:

Received October 12, 2024

Received in revised form

November 25, 2024

Accepted March 22, 2025

Available online

March 22, 2025

Keywords:

Alkaloids

Regioselectivity

intramolecular

DFT

Plasmodium Falciparum

Docking and molecular

dynamics

ADMET

ABSTRACT

This study examines the reactivity of an intramolecular cyclization process involving benzastatin, a molecule derived from *Streptomyces nitrosporeus*, using density functional theory (DFT) with the B3LYP functional and the 6-311G(d,p) basis set. Parr indices, calculated by natural bond orbital (NBO) analysis, provide insight into the reactivity and chemical behavior of the system. In addition, the electron localization function (ELF) is used to analyze bond formation during the process. A molecular docking study highlights the pharmacological potential of benzastatin-derived alkaloids against *Plasmodium falciparum*, the malaria parasite, by targeting the key enzymes falcipain-2 and falcipain-3. The study elucidates the key interactions and binding affinities between the reaction products involved and these enzymes, supported by molecular dynamics simulations to study the stability of the ligand-protein complex over 50 ns. ADMET predictions suggest favorable pharmacokinetic profiles and low toxicity for the compounds, underlining their potential as antimalarial drug candidates.

© 2025 by the authors; licensee Growing Science, Canada.

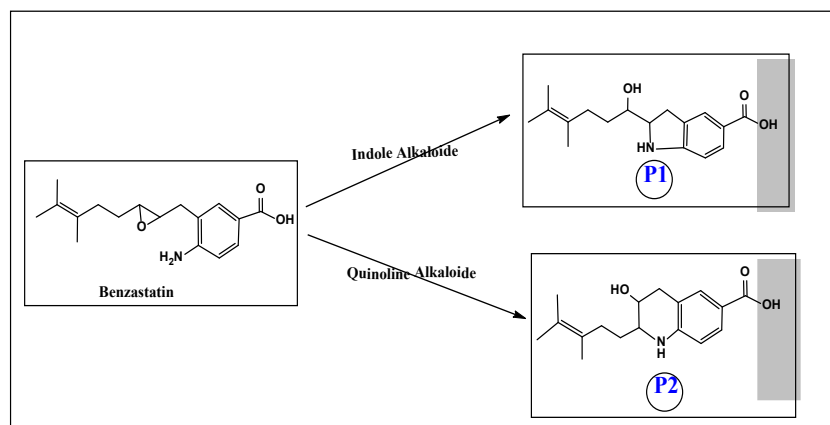
1. Introduction

Alkaloids are a broad class of natural molecules, synthesized mainly from amino acids. Their structural and functional diversity makes them compounds of great chemical and biological interest.¹ Among these molecules, quinolines and indoles stand out for their remarkable pharmacological properties, particularly in the treatment of malaria.^{2,3} Quinolines, characterized by a bicyclic nitrogen ring, have historically played a key role in the fight against this disease, with emblematic compounds such as quinine and Cinchonine.⁴ Indole derivatives, meanwhile, have also shown promising antimalarial activity against chloroquine-resistant strains of *Plasmodium*, by inhibiting hemozoin formation via a different mode of action to chloroquine.⁵ In addition to their antimalarial properties, these two families of alkaloids display a wide range of biological activities, including anticancer,^{6,7} antifungal,⁸ antibacterial^{9,10} and antiviral activity,^{11,12} making them ideal structural scaffolds for pharmacological research.

Despite the progress made in the fight against malaria, the disease remains a major challenge due to the emergence of resistance to conventional treatments.^{13,14} This situation has led to an intensification of research aimed at discovering new therapeutic agents and better understanding the molecular mechanisms underlying their activity. In this context, theoretical approaches play a crucial role in exploring and optimizing new synthetic pathways and identifying new bioactive compounds. Methods such as DFT, molecular docking and ADMET enable us to assess reaction mechanisms, regio- and stereoselectivity, predict biological affinity, and examine the pharmacokinetic and toxicological properties of compounds to ensure their efficacy and safety.

* Corresponding author

E-mail address zeroualabdellah2@gmail.com (Z. Abdellah)



Scheme 1. The two possible products resulting from the intramolecular reaction of a benzastatin alkaloid

Indeed, the present work is part of a theoretical study of the intramolecular cyclization reaction of a benzastatin (Scheme 1), an alkaloid derivative isolated from *Streptomyces nitrosporeus*. The quinoline and indole derivatives resulting from the reaction were then subjected to molecular docking analysis on falcipain-2 (FP-2) and falcipain-3 (FP-3), vital proteases in the life cycle of *Plasmodium falciparum*, responsible for malaria in humans. The work is complemented by molecular dynamics and ADMET prediction studies to analyze, respectively, the stability of the best-proposed protein-ligand complex and the pharmacokinetic and toxicological properties of the two products.

2. Calculation methodology

2.1 chemical reactivity

Herein we investigated the chemical reactivity and selectivity of the intramolecular reaction of the benzastatin derivative using density functional theory (DFT). We computed the DFT using the GaussView-6.0 graphical interface¹⁵ and the GAUSSIAN 09 software.¹⁶ Especially, the B3LYP functional¹⁷ approach with the 6-311G(d,p) basis set¹⁸ was applied to maximize the geometry of the stationary points, comprising reactants, transition structures, and products. To guarantee their stability, frequency computations were performed to verify the lack of any imaginary frequency at minima and the presence of a single imaginary frequency at transition structures. N,N-Dimethylformamide (DMF) was used as solvent using a self-consistent reaction field (SCRF) based on Tomasi's polarizable continuum model (CPCM).¹⁹⁻²³ Additionally, included in the study was the Parr function²⁴ examination of local and global responsiveness. Calculated using the formula stated in,²⁵ the global reactivity indices, electronic chemical potential (μ), chemical hardness (η), global electrophilicity (ω), and global nucleophilicity (N) were computed to describe the reactivity of the molecular systems. Multiwfn program²⁶ was used for ELF topological investigation.

2.2 Molecular docking

The biological activity of our compounds was evaluated by molecular docking using AutoDock Vina software,²⁷ targeting the falcipain-2 (FP-2) and falcipain-3 (FP-3) enzymes of *Plasmodium falciparum* (PDB codes: 3BPF and 3BPM,²⁸ key targets in the fight against malaria. Ligands were prepared with AutoDock Tools²⁹ and converted to .PDBQT format. Proteins were prepared under a Linux environment using UCSF Chimera,³⁰ with the "Surface/Binding Analysis" option. Docking calculations were performed under Windows with AutoDock Vina, requiring .PDBQT files for both ligand and protein. Ligand-protein interactions were visualized using Discovery Studio.³¹

2.3 Molecular dynamics

Molecular dynamics simulation was carried out with GROMACS.³² The topology file of the docked product was generated using the SwissParam tool.³³ The CHARMM27 force field³⁴ was applied to the system to perform the MD simulation. A box of TIP3P-type water molecules³⁵ was created with a distance of 1.0 nm between the edge of the box and the protein, forming the environment of the protein-ligand system. An appropriate number of counterions were added to neutralize the system. The system was then equilibrated using NVT and NPT sets for 5 ns. MD simulation was performed for a 50 ns production run with a time step of 2 fs (femto-second), maintaining a constant pressure of 1 atm and a constant temperature of 300 K. Snapshots were recorded every 2 picoseconds (ps). Various parameters, such as root mean square deviation (RMSD), root mean square fluctuation (RMSF), radius of gyration (Rg), hydrogen bond (HB) and solvent accessibility surface area (SASA), were analyzed using GROMACS to assess the conformational stability of the complex in a dynamic environment. The results were visualized with Xmgrace.³⁶

3. Results and discussions

3.1 chemical reactivity and indices

3.1.1 Global reactivity indices

The B3LYP/6-311G(d,p) optimized geometry of benzastatin is represented in **Fig. 1**.

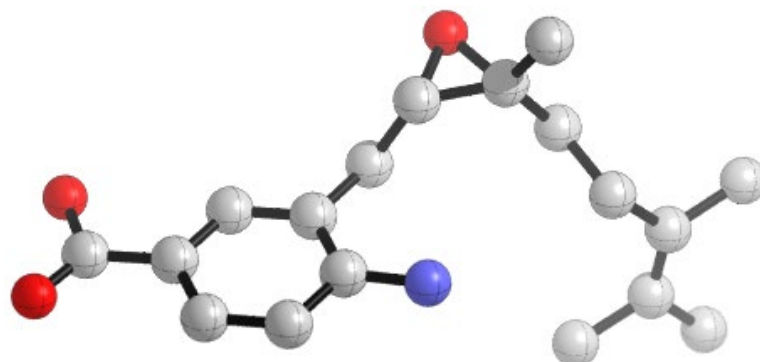


Fig. 1: Optimized Geometry of the benzastatin

Table 1. The energies of HOMO and LUMO, μ , η , ω and N in eV

HOMO	LUMO	μ	η	ω	N
-0,23	-0,04	-3,62	4,99	1,31	3,25

The initial compound (reagent) presents the electronic chemical potential μ of -3.62 eV and global hardness 4.99 eV, and the global electrophilicity index of 1.31 eV ($0.80 \leq \omega \leq 1.50$), classifying it as a moderate electrophile within the standard electrophilicity scale.³⁷ The nucleophilicity index N value of 3.25 eV ($N > 3.00$ eV) classified the compound as a strong nucleophile within the standard nucleophilicity scale.³⁸

3.1.2 Prediction of the regioselectivity

Determining the nucleophilicity and electrophilicity of reactants in intramolecular reactions presents an additional difficulty, since both reacting counterparts exist in a single molecule. This problem can be solved by using an appropriate technique to split the molecule into three parts as depicted in **Fig. 2**.

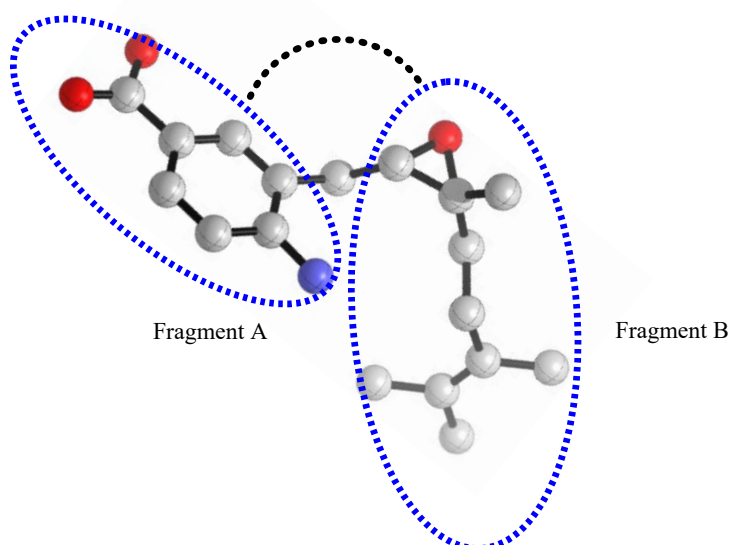


Fig. 2. Fragmentation of benzastatin

We have proposed two regions A and B in the present system which can be considered as an inhomogeneous electron gas, this principle is used in some works, the Tachibana model and al.³⁹⁻⁴¹, which considers that the two regions A and B

change the heat, the work and the electrons in the molecule. In this work we define three zones, corresponding to the fraction A which represents the nucleophilic part, the fragment B which is the zone of the epoxide and the CH₂ chain which connects the two fragments.⁴² The CH₂ chain acts as a bridge between the two fragments within the molecule. It is worth mentioning that this partition is similar to that shown in some Diels Alder intramolecular reactions, which shows that the contribution of the intramolecular reactivity of the methylene chain is negligible. Thus, Tachibana³⁰ suggested in his model that the chain of union plays the role of disruptive agent. He noted that the unperturbed system naturally becomes an intermolecular interaction between fragments A and B. The local reactivity indices (ω_k and N_k) are reliable indicators for the prediction of the most favored interaction during a chemical reaction. The most favorable regioisomer is the one associated with the largest local electrophilicity index ω_k of the electrophile and the largest local nucleophilicity index N_k of the nucleophile. We analyzed the N_k value and the ω_k value for the reactant to predict the most likely electrophile/nucleophile interaction along the reaction path to explain the regioselectivity of the reaction.

In order to predict the regioselectivity of the reaction, analysis of the Parr functions was performed, which constitute crucial

local parameters for studying regioselectivity. The Parr functions $P(r)$, introduced by Domingo,^{24,43} are defined by the following equations:

$$P^-(r) = \rho_s^{rc}(r) \text{ For an electrophilic attack} \quad (1)$$

$$P^+(r) = \rho_s^{ra}(r) \text{ For a nucleophilic attack} \quad (2)$$

$\rho_s^{rc}(r)$ and $\rho_s^{ra}(r)$ are respectively ASD (Atomic Spin Densities) of a considered atom r, whether anionic or cationic.

$$\omega_k = \omega P_k^+ \quad (3)$$

$$N_k = N P_k^- \quad (4)$$

ω_k and N_k represent, respectively, local electrophilicity and local nucleophilicity. We have adopted the two-center approach proposed by Domingo, which allows predicting the favorable isomer. According to this method, the formation of the first bond is attributed to the interaction between the most electrophilic site (identified by the highest value of ω_k) and the most nucleophilic site (defined by the highest value of N_k). Predicting the formation of the first bond proves sufficient to anticipate the preference of the resulting isomer. The values of local electrophilicities ω_k and nucleophilicities N_k , listed in **Tables 1** and **2**, allow characterizing the most favorable interaction.

Table 2. Electrophilic and Nucleophilic Parr Functions

Fragment A				Fragment B			
$\sum_{k \in A} P_k^+$	$\sum_{k \in A} P_k^-$	ω_A	N_A	$\sum_{k \in B} P_k^+$	$\sum_{k \in B} P_k^-$	ω_B	N_B
0.031	0.867	0.040	2.817	0.335	0.042	0.439	0.138

The results from **Table 2** reveal that fragment A acts as a nucleophile, given that NBO calculations of local indices indicate that N_A is significantly higher than N_B . Simultaneously, we observe that fragment B exhibits a higher electrophilicity value compared to fragment A, indicating that fragment B is electron-deficient, while fragment A is electron-rich.

Table 3. Electrophilic and Nucleophilic Parr Functions

	P_k^+	P_k^-	ω_k	N_k
N	0.207	0.025	0.272	0.081
C18	0.005	-0.004	0.007	-0.013
C21	0.001	0.003	0.001	0.010

Analysis based on local electrophilicity ω_k and nucleophilicity N_k , through Natural Bond Orbital (NBO) analyses using Parr function indices, reveals that carbon C18 exhibits a higher electrophilic character relative to carbon C21 (Figure 3). This suggests that the opening of the epoxide will occur through a nucleophilic attack by nitrogen on carbon C18. These results explain the preferred generation of regioisomer P1 is the favored product, even though it contradicts the thermodynamic results. Indeed, product P2, with the quinoline core, is thermodynamically more favorable. This suggests

that Parr's indices, while useful for predicting reactivity trends, are not sufficiently precise to fully explain the observed regioselectivity of the reaction.

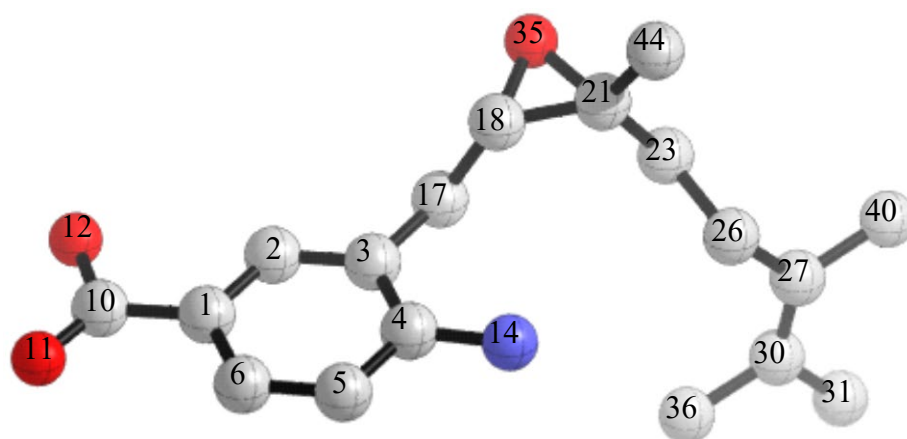


Fig. 3. Numbering benzastatin atoms

3.1.3 Prediction of the direction of the electron flow using the indices of duels

The direction of electron flow can be determined using the dual indices γ_1 and γ_2 ⁴⁴ defined as follows. $\gamma_1 = \omega_B + N_A$, and $\gamma_2 = \omega_A + N_B$. If $\gamma_1 > \gamma_2$, charge transfer will take place from fragment A to fragment B. If $\gamma_1 < \gamma_2$, charge transfer will take place from fragment B to fragment A. If $\gamma_1 = \gamma_2$, there is a chemical equilibrium between the two fragments (CT= 0). The values obtained are reported in **Table 4**.

Table 4. Dual indices γ_1 and γ_2

γ_1 (eV)	γ_2 (eV)	$\Delta\gamma_{12}$ (eV)
3.11	1.24	1.87

According to the results of **Table 4**, we find that $\gamma_1 > \gamma_2$, then the charge transfer will take place from fragment A to fragment B (A \rightarrow B), which confirms the results found by calculating the Fukui indices. This transfer of charge from A to B is due to the presence of the nitrogen atom of fragment A which has a nucleophilic character (electron donor). So the latter will attack the carbons forming the epoxide of fragment B, which have an electrophilic character to form either a five-membered ring structure or a six-membered ring structure. Furthermore, we notice that $\Delta\gamma_{12}$ is slightly significant; this means that the reaction is a weak polar reaction. In order to know and confirm the percentage transfer of nucleophilicity and electrophilicity between the two fragments, we performed calculations of the degree of transferability of each fragment; the results are collected in **Tables 5** and **6**.

Table 5. Degree of transferability T_ω

ω_A (eV)	ω_B (eV)	ω (eV)	$\%(T_{\omega A} = \omega_A / \omega)$	$\%(T_{\omega B} = \omega_B / \omega)$
0.69	0.58	1.31	52.17	44.41

Table 6. Degree of transferability T_N

N_A (eV)	N_B (eV)	N (eV)	$\%(T_{N A} = N_A / N)$	$\%(T_{N B} = N_B / N)$
2.53	0.56	3.25	77.74	17.18

Referring to the results of **Tables 5** and **6**, we note that nucleophilic character is concentrated at the fragment A, which has a nucleophilic character of 78%. Therefore, the electron transfer will take place from fragment A to fragment B.

3.1.4 Study of the mechanism of the reaction

The transition states **TS1** and **TS2** corresponding to the two Regioisomers P1 and P2 were located by following the potential energy surface (PES) at the B3LYP/6-311G (d,p) computational level. The two transition states were confirmed

by the presence of a single negative value in the matrix of force constants; there is a single imaginary frequency in the Hessian matrix which corresponds to the mode of vibration equivalent to the formation of a new C-N bond and the breaking of the C-O bond. The optimized geometry of the TSs **TS1** and **TS2** associated with the generation of products **P1** and **P2** are represented in **Fig. 4**.

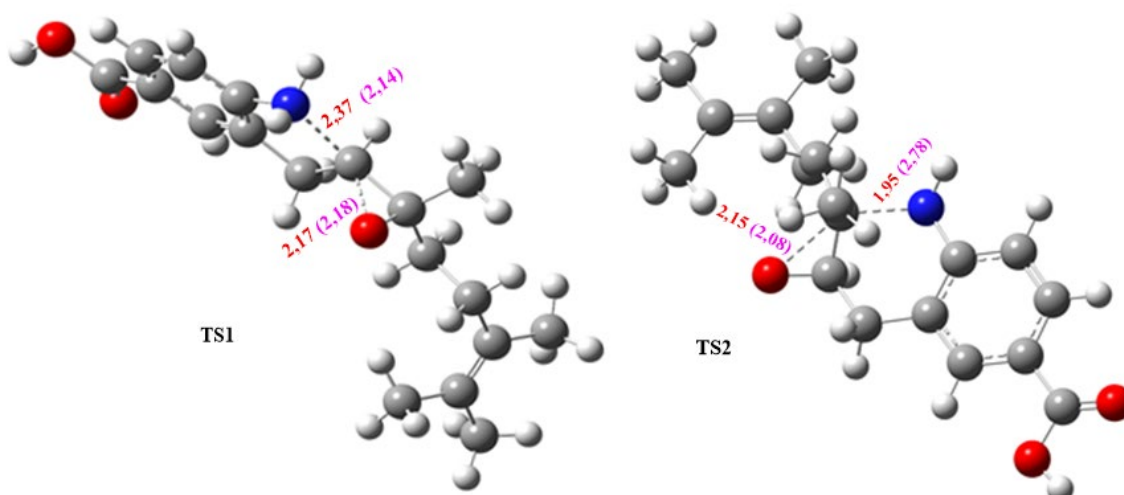


Fig. 4. Distances of the bonds (Å) for the transition states of the reaction in a gaseous medium and in the DMF in parentheses.

According to the results presented in **Fig. 4**, we notice for **TS1** the formation of the Nitrogen-Carbon bond forming the five-membered ring structure, with an interatomic distance of 2.37 Å and the breaking of the Carbon-Oxygen bond of the epoxy with the distance of 2.17 Å as for **TS2**, there is formation of the Nitrogen-Carbon bond leading to the formation of six-membered ring structure, with a distance of 1.95 Å and rupture of the Carbon-Oxygen bond of the epoxide with the distance of 2.15 Å. These two transition states are indeed related to the two minima. The analysis of the reaction path described by IRC is detailed in the supplementary data.

3.1.5 Analysis of the potential energy surface and prediction of the reaction mechanism

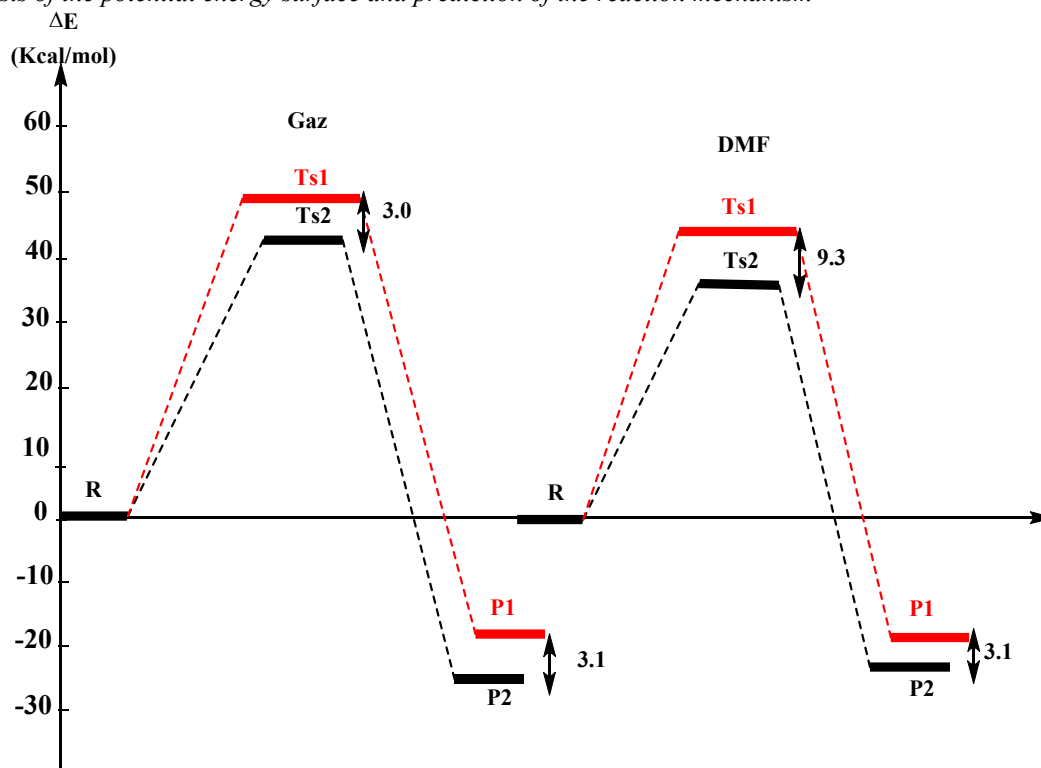


Fig. 5. Energy profile of the reaction in a gas medium and in the presence of DMF at the B3LYP/6-311G level (d, p)

The energy profile along the potential energy surface (PES) for the two regioisomeric reaction channels of the intramolecular reaction of benzastatine, is shown in **Figure 5**. In the gas phase, the transition state **TS2** shows activation energy of 42.9 kcal/mol, is located 3.0 Kcal/mol below **TS1**. In addition, the product **P1** is located 3.1 kcal/mol above **P2**.

Therefore, the **P2** regioisomer is kinetically and thermodynamically more favored in the gas phase relative to the **P1** regioisomer. In the presence of DMF as solvent, slight change is observed in the energy profile. The activation energy of **TS2** is 35.8 kcal/mol, located 9.3 kcal/mol below **TS1**, and the product **P1** is located 3.1 kcal/mol above **P2**. Therefore, it can be concluded that the reaction is energetically more feasible in DMF relative to the gaseous medium. Based on these results, we conclude that regioisomer **P2** is kinetically and thermodynamically favorable in the gas phase and in DMF.

3.1.6 Thermodynamic study of the reaction

Table 7. The thermodynamic quantities characterising the intramolecular cyclization reaction of the reactant (benzastatin) and the energies corresponding to the transition states and products formed in DMF (the relative values are given in Kcal/mol)

	TS1	TS2	P1	P2
ΔE	45.1	35.8	-18.5	-21.6
ΔH	42.4	34.7	-18.0	-20.9
ΔG	43.9	36.0	-17.3	-19.9

The products **P1** and **P2** obtained are highly exothermic, with values of -18.5 Kcal/mol and -21.6 Kcal/mol respectively. This confirms that **P2** is thermodynamically favoured over **P1**. In DMF, the results obtained are slightly different from those found in the gas phase, implying that the solvent does not have a major effect on the course of the reaction.

3.2 ELF topological analysis

The topological analysis of the ELF function allows a partition of the molecular space into basins of electronic localization within which the excess of kinetic energy due to the Pauli repulsion is minimum.^{45,46} The special position of these attractors makes it possible to differentiate between core basins and valence basins. Core basins are located around the nuclei. Valence pools are classified according to their connectivity with core pools, and this defines the synaptic order. A large body of theoretical work on cyclization reactions has shown that electron localization function (ELF)⁴⁷ bond analysis along the IRC is an important tool for understanding the bonds that form or break along the reaction path. ELF provides basins in which the probability of finding an electron pair is maximum.

Table 8. Classification of ELF basins according to synaptic order

Synaptic Order	Nomenclature	Symbol	Chemical significance
1	Monosynaptic	V(X)	Free pair
2	Disynaptic	V(X, Y)	Covalent bond
≥ 3	Polysynaptic	V(X, Y, ...)	Multicentric bond

In this work we carried out a complete analysis of the ELF along the IRC of the product **P2**, in order to better explain the formation of the sigma N-C bond formed and the breaking of the C-O bond of the epoxide during the reaction. This ELF topological analysis made through IRC data is directly associated with the most favorable reaction path. The electronic populations of the most significant ELF valence basins of the selected structures along the IRC profile are given in **Table 9**.

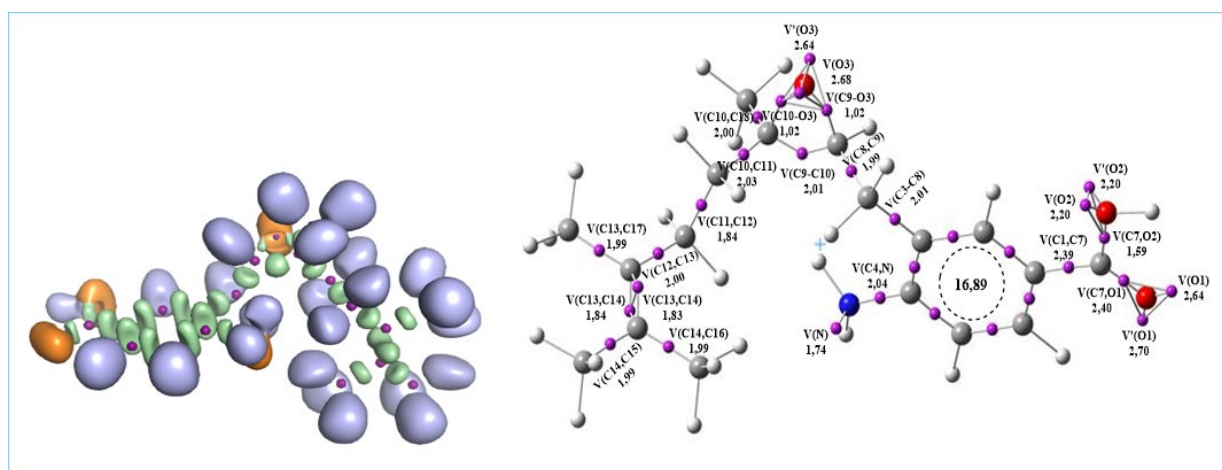


Fig. 6. Representative figure of the ELF pools of the reagent accompanied by the electronic populations.

The ELF topology for **Fig. 6** shows the oxygen atom **O3** of the epoxide carries two monosynaptic basins **V(O3)** and **V'(O3)** with a total electron population of 5.32 e, more than 4e, which shows the existence of two lone electron pairs, with a slight electron density as a radical electron. The presence of the **V(N)** monosynaptic basin on the **N** atom integrates 1.74e

implies that there is a bondless region around the N atom equivalent to a lone pair of electrons. The C4-N bond is characterized by the presence of a disynaptic basin $V(C4, N)$ reaching 2.04e which is slightly higher than 2e, reveals a single bond with a slightly double character for the region C4-N.

Table 9. Populations of the valence basins obtained by ELF calculation of certain selected points along the IRC curve for the product P2.

	First step						Second step		
	P1	P13	P18	P21	P33	P42	P46	P53	P77
PBV	P0	P1	P2	P3	P4	P5	P6	P7	P8
d(C5-N)	5.45	5.13	4.87	4.69	3.91	3.21	2.99	2.93	2.93
V(N)	1.79	1.87	0.44	1.94	1.78	--	--	--	--
V'(N)	--	--	2.28	--	--	--	--	--	--
V(C4-N)	2.01	1.95	1.46	1.89	1.83	1.83	1.83	1.84	1.84
V(C3-C2)	1.98	1.99	1.90	2.00	1.83	2.06	2.06	2.06	2.05
V(C2-C1)	2.02	2.02	1.91	1.99	1.95	1.93	1.93	1.93	1.93
V(C1-O3)	1.02	1.03	0.91	1.13	1.30	1.47	1.50	1.52	1.53
V(C1-C5)	1.99	2.00	2.02	2.10	2.25	2.08	2.03	2.01	2.00
V(O3)	2.66	2.66	2.83	2.87	2.97	2.42	2.46	2.51	2.52
V'(O3)	2.67	2.67	2.87	3.29	3.05	3.66	3.61	3.53	3.53
V(C5-O3)	1.03	1.02	0.68	--	--	--	--	--	--
V(C5-C11)	2.02	2.03	1.95	2.06	2.08	1.99	1.97	1.96	1.97
V(C5-C18)	2.01	2.00	1.93	2.03	2.04	1.98	1.96	1.96	1.96
V(C5-N)	--	--	--	--	--	1.72	1.75	1.77	1.77

Understanding the molecular mechanism of this reaction requires in-depth study by the ELF method. The study was carried out for the majority regioisomer (P2) in the ground state in the gas phase. To this end, ELF analysis was carried out on the most relevant points along the IRC profile for **TS2**, connecting the two fragments of the molecule. Attractor positions for the most relevant points associated with C5-N single bond formation and C5-O3 single bond breaking are shown in the **Table 9**, while electronic populations of the most ELF valence basins relevant structures selected along the IRC profile are listed in the table. According to the results displayed in **Table 9**, we can derive the following information; these 9 chosen points of analysis are the most significant and reveal very interesting information. For **P0**, we have two important monosynaptic basins $V(O3)$ and $V'(O3)$ with a population sum equal to 5.33e which corresponds to the two lone pairs of the oxygen atom of the epoxide and in addition from this we have another monosynaptic basin $V'(N)$ with a population of 1.79e corresponding to the nitrogen lone pair. We also observed the presence of several disynaptic basins, but the most important is $V(C5-O3)$, integrating 1.03e, a single bonding character for C5-O3. A critical point is observed at the level of P2, where one observes the appearance of a monosynaptic basin at the N atom integrating 2.28e, allowing the preparation for the formation of a new sigma N bond. In the P3 level, we observe the disappearance of a disynaptic basin $V(C5-O3)$, which implies the rupture of the C5-O3 single bond which corresponds to the starting epoxide. In addition, in the P3-P4 interval, we noticed a significant decrease in the distance $d(C5-N)$, a rapprochement of the two atoms for a possible nucleophilic attack of the nitrogen atom with the carbocation formed. In the second stage, the most relevant point is P5, where we observe the appearance of a new disynaptic basin between C5 and N atoms with a population of 1.72e, which explains the formation of the new single bond C5-N, forming the 6-membered ring. At the same time, we observe the depopulation or disappearance of the monosynaptic basin $V(N)$, which confirms an electronic split between N and C5.

3.3 Molecular docking

3.3.1 Research into the interactions of our products with target proteins: Falcipaine-2 (PDB ID: 3BPF) and Falcipaine-3 (3BPM)

Molecular docking is a method that calculates the preferred orientation of one molecule over another when they are linked to form a stable complex with good affinity.⁴⁸ Computer-aided drug design plays a very important role in the development of selective and potent inhibitors and vaccines. Molecular docking is one of the approaches used in drug design and discovery.^{49,50} Malaria is a disease caused by parasites of the genus *Plasmodium*. According to a WHO report, in 2024, the disease had already affected around 263 million people worldwide, causing over 597,000 deaths.⁵¹ Moreover, widespread drug resistance is increasingly limiting the efficacy of available therapies. Consequently, identifying new targets for a new drug discovery process is an urgent priority. In this context, falcipain-2 and falcipain-3 in *P. falciparum* represent key enzymes in the parasite's life cycle.^{28,52}

Falcipain-2 and falcipain-3 are involved in hemoglobin hydrolysis, an essential pathway to supply free amino acids for the parasite's metabolic needs. Furthermore, falcipain-2 is involved in the cleavage of ankirin. In this part of our work, we tested the inhibitory capacity of our products, P1 and P2 against the two hemoglobinases of *plasmodium falciparum*, FP-2 and FP-3, considered as key enzymes. Disruption of these enzymes results in reduced hemoglobin hydrolysis, i.e.

reduced parasite potency. We used chloroquine as our reference drug, as the parasite is sensitive to chloroquine.⁵³ The latter will enable us to classify the level of efficacy of our products.

3.1.1.1 Interactions between ligands and amino acid residues

A- Ligands-FP2

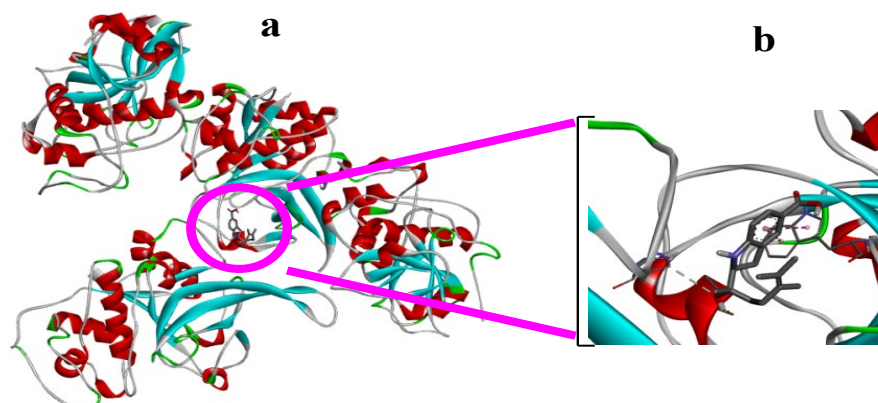


Fig. 7. P1 product docked in the falcipain-2 protease (PDB ID: 3BPF) with (a) P1 in complex in the best position of the catalytic site (b) Zoom of the P1 interaction with the protease.

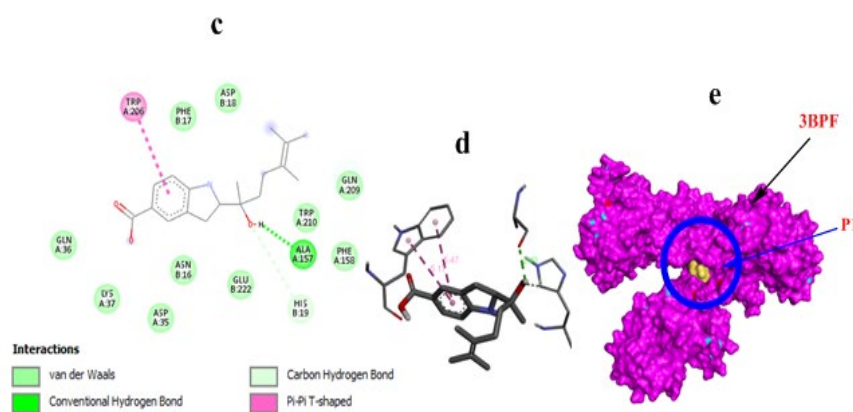


Fig. 8. P1 product docked in the falcipain-2 protease (PDB ID: 3BPF) with (c) Interactions of P1 with FP-2 amino acids, with one hydrogen bonding (dark green dotted lines), (d) Amino acid residues involved in interaction with P1 (ligand in dark sticks), and (e) Best mode of ligand binding in the protein pocket (P1 in yellow).

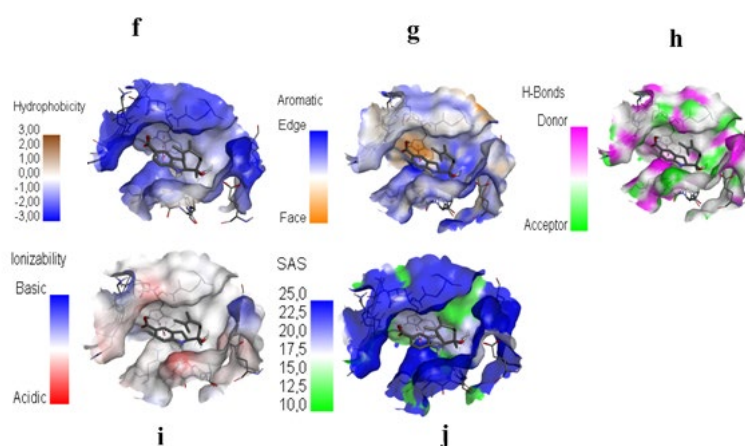


Fig. 9. Surface representations of the different types of binding of the active site of the falcipain-2 protein (PDB ID: 3BPF) around the ligand P1 (f) Hydrophobic binding surface (in blue), (g) Surface of aromatic bonding (in blue aromatic border interaction and in orange facial aromatic interaction), (h) Hydrogen bonding surface (in green the acceptor side, in pink the donor side and in white the neutral side), (i) Acid-base binding surface (in blue strong basicity, in red strong acidity), and (j) Solvent accessibility surface of the active site of the protein around P1 (in blue strong solvent accessibility, in green no accessibility and in white low accessibility).

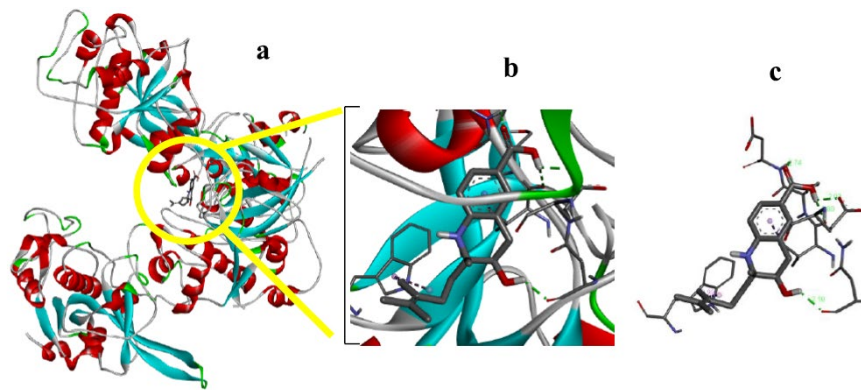


Fig. 10. P2 product docked with the falcipain-2 protease (PDB ID: 3BPF) with (a) P2 in complex in the best position of the catalytic site, (b) Zoom of the P2 interaction with the protease and (c) Amino acid residues involved in the interaction with P2 (dark rod ligand).

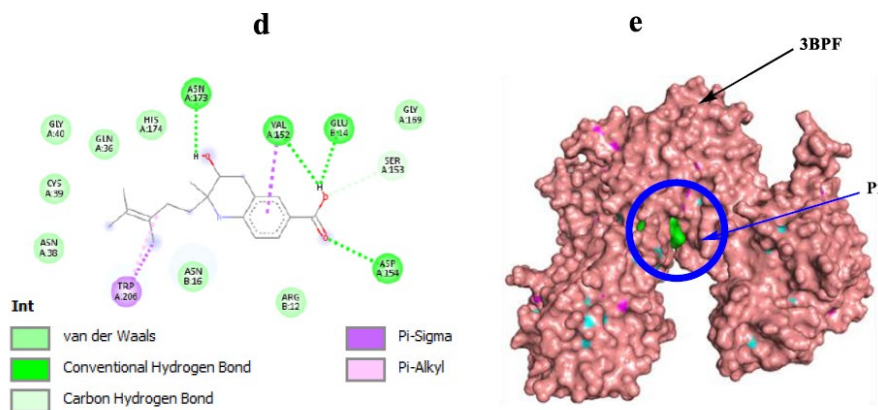


Fig. 11. Docked P2 product with falcipain-2 protease (PDB ID: 3BPF) with (d) P2 interactions with FP2 amino acids, 4 hydrogen bonds (dark green dotted lines), and (e) Best ligand binding mode in the protein pocket (P2 shown in green).

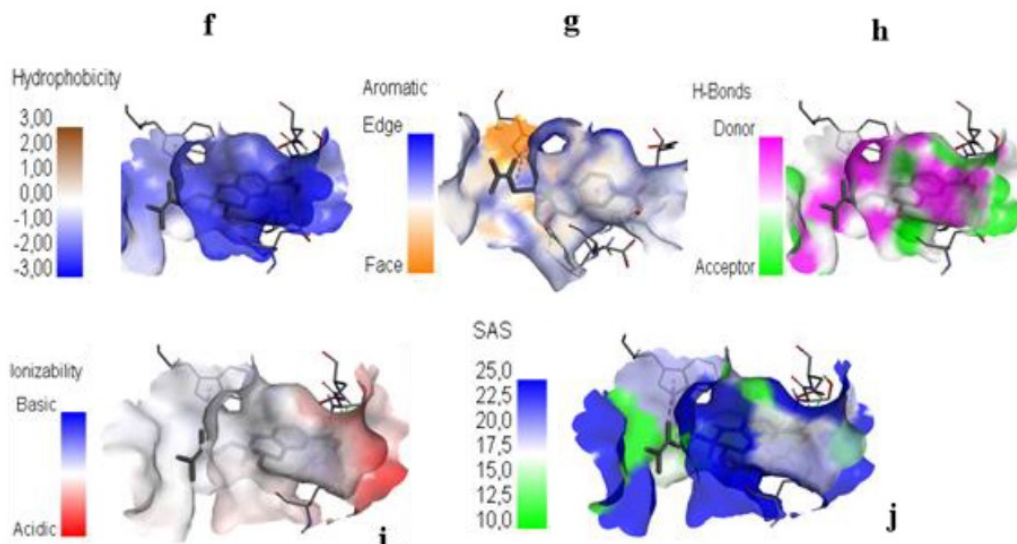


Fig. 12. Surface representations of the different binding types of the falcipain-2 protein active site (PDB ID: 3BPF) around the P2 ligand, (f) Hydrophobic binding surface (in blue), (g) Aromatic binding surface (in blue aromatic border interaction and in orange facial aromatic interaction), (h) Hydrogen bonding surface (in green the acceptor side, in pink the donor side and in white the neutral side), (i) Bonding surface acid-base (in blue strong basicity, in red strong acidity), and (j) Solvent accessibility surface of the active site of the protein around P2 (in blue strong accessibility to solvent, in green no accessibility and in low accessibility white).

According to the 2D and 3D structures in **Figs. 7-12**, we have several types of interactions formed between the P1, P2 ligands and the FP-2 protein. The molecular docking scores of the ligands and amino acids found in the site's assets of the

FP-2 enzyme are shown in **Table 10**. The observation of interactions between amino acid residues aims to identify the interactions that occur between ligands and receptor. These interactions occur in the form of hydrogen bonds, hydrophobic interactions, and electrostatic interactions. The results of the molecular docking on the FP-2 enzyme show that there is no similar interaction between the comparison ligand and our bioactive compounds.

Table 10. Results of affinity energies, ligands-FP3 interactions and distances of interactions

Ligands	Affinity energies	Amino acids	Interactions	Distances
Chloroquine-FP2	-5,2 Kcal/mol	VAL C:71	H-bond	2,78 Å
		ASP C:72	C-H-bond	3,41 Å
		TYR C:78	C-H-bond	3,59 Å
			Pi-Amide	4,65 Å
P1- FP2	-6,7 Kcal/mol	TRP A:206	Pi-Alkyl	4,68 Å
			Pi-Pi T-shaped	5,17 Å
		ALA A: 157	H-bond	2,56 Å
		HIS B: 19	C-H-bond	3,42 Å
		GLU B:14	H-bond	2,03 Å
P2- FP2	-8,2 Kcal/mol	VAL A:152	H-bond	2,80 Å
		SER A:153	Pi-Sigma	3,71 Å
			C-H-bond	2,99 Å
		ASP A:154	H-bond	2,74 Å
		ASN A:173	H-bond	2,10 Å
		TRP A:206	Pi-Sigma	3,71 Å
			Pi-Alkyl	5,38 Å

For P1, the interactions formed with FP-2 residues are of several types: a hydrogen interaction is formed with ALA 157, a C-H interaction with HIS 19, a Pi-Pi-T-shaped interaction with TRP 206 and weak Van der Waals interactions involving several amino acids. And for P2 with the same receptor, 4 hydrogen interactions are formed with residues GLU 14, VAL 152, ASP 154, ASN 173, three hydrophobic interactions with residues VAL 152 and TRP 206, a C-H interaction with SER 153 and Van der Waals interactions. The amino acid common to both complexes is TRP 206.

B-Ligands-FP3

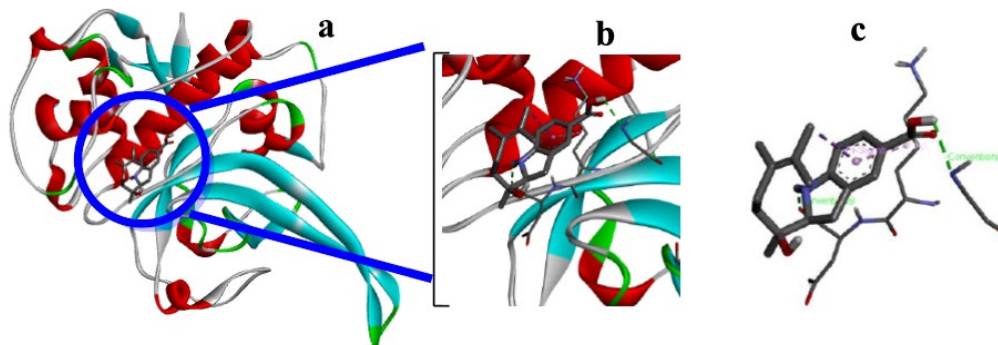


Fig. 13. P1 product docked with falcipain-3 protease (PDB ID: 3BPM) with (a) P1 in complex in the best position of the catalytic site, (b) Zoom of the P1 interaction with the protease and (c) Amino acid residues involved in the interaction with P1 (ligand in rods dark).

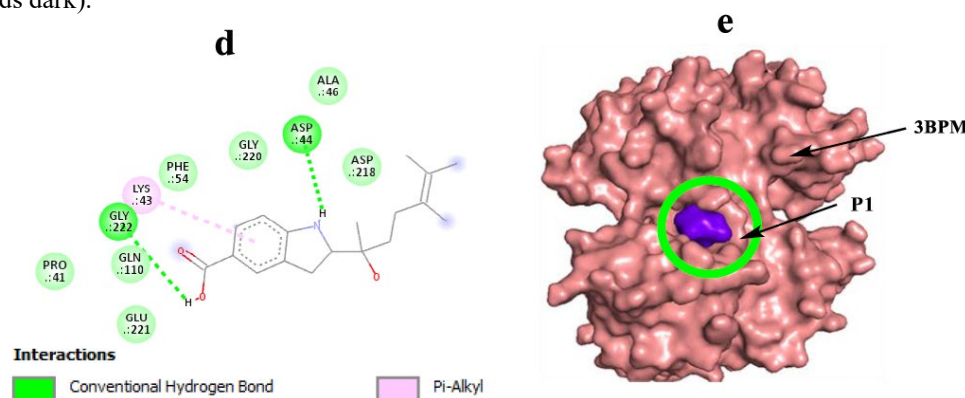


Fig.14. P1 product docked with falcipain-3 protease (PDB ID: 3BPM) with (d) Interactions of P1 with the amino acids of FP3, with 2 hydrogen bonds (in green dotted lines dark), and (e) Best ligand binding mode in the protein pocket (P1 shown in purple).

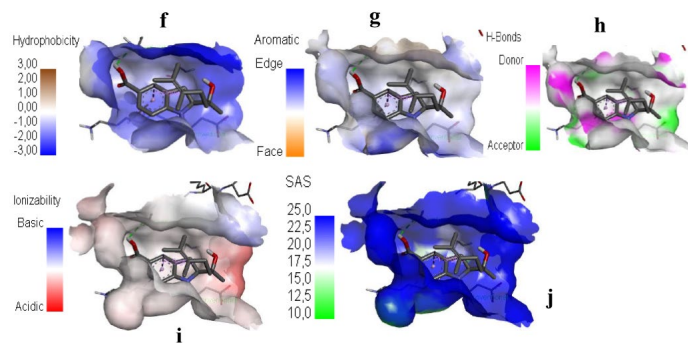


Fig. 15. Surface representations of different protein active site binding types of falcipain-3 (PDB ID: 3BPM) around ligand P1 (f) Hydrophobic binding surface (in blue), (g) Aromatic binding surface (in blue edge aromatic interaction and in orange facial aromatic interaction), (h) Hydrogen bonding surface (in green the side acceptor, in pink the donor side and white the neutral side), (i) Acid-base binding surface (in strong basicity blue, in strong acidity red), and (j) Solvent accessibility surface of the active site of the protein around P1 (in blue, high solvent accessibility, in green, no accessibility and in low accessibility white).

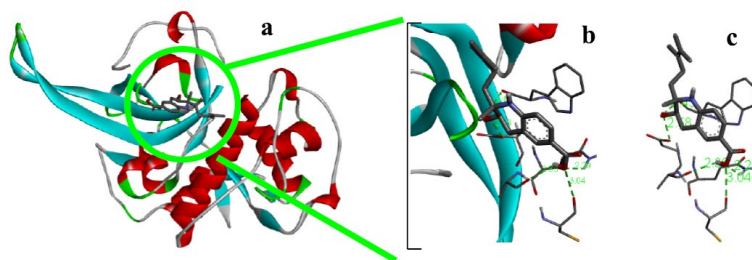


Fig. 16. P2 product docked with falcipain-3 protease (PDB ID: 3BPM) (a) P2 in complex in the best position of the catalytic site, (b) Zoom of the P1 interaction with the protease and (c) Amino acid residues involved in the interaction with P2 (ligand in rods dark).

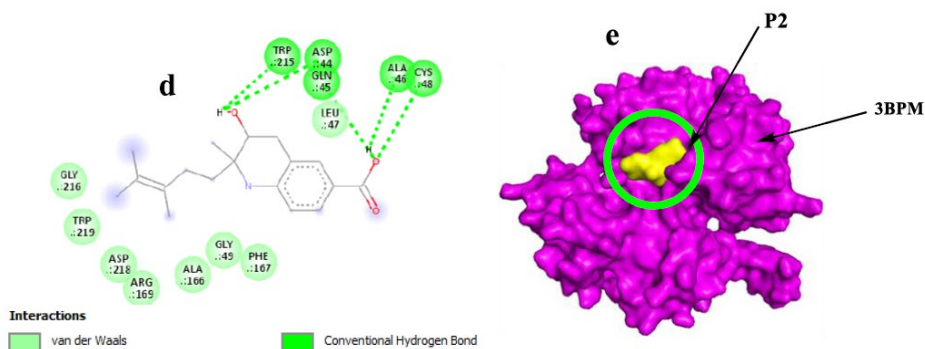


Fig. 17. P2 product docked with falcipain-3 protease (PDB ID: 3BPM) with (d) Interactions of P2 with the amino acids of FP3, 5 hydrogen bonds (in green dotted lines dark), and (e) Best binding mode of the ligand in the pocket of the protein (P2 represented in yellow).

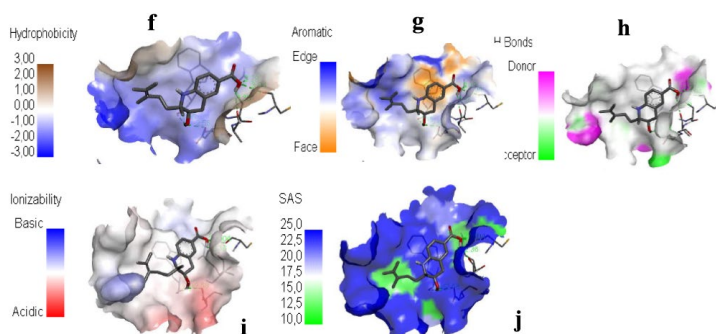


Fig. 18. Surface representations of different types of protein active site binding of falcipain-3 (PDB ID: 3BPM) around the P2 ligand (f) Hydrophobic binding surface (in blue), (g) Aromatic binding surface (in blue edge aromatic interaction and in orange facial aromatic interaction), (h) Hydrogen bonding surface (in green the side acceptor, in pink the donor side and white the neutral side), (i) Acid-base binding surface (in strong basicity blue, in strong acidity red), and (j) Solvent accessibility surface of the active site of the protein around P2 (high solvent accessibility in blue, no accessibility in green and in white low accessibility).

According to the 2D and 3D structures in Figures 13-18, we have several types of interactions formed between the P1, P2 ligands and the FP3 protein. The molecular docking scores of the ligands and amino acids found in the active sites of the FP3 enzyme are shown in Table 11. The results of the interaction between the FP-3 receptor and the P1 and P2 ligands showed two types of interactions that occur with amino acids. For P1, we have the amino acids ASP 44, GLY 222 which form hydrogen type interactions and LYS 43 a Van der Waals type interaction. And P2 forms five hydrogen-like interactions with amino acids ASP 44, GLN 45, ALA 46, CYS 48 and TRP 215. The common amino acid for both complexes is ASP 44. These results show that the compounds P1 and P2 are compounds which have the potential to be used as inhibitors of the Falcipain-2 and Falcipain-3 receptors of the *Plasmodium Falciparum* parasite, responsible for human malaria.

Table 11. Results of affinity energies, ligands-FP3 interactions and distances of interactions

Ligands	Affinity energies	Amino acids	Interactions	Distances
Chloroquine-FP3	-5,6 Kcal/mol	VAL :80	H-bond	2,59 Å
		SER :83	C-H-bond	3,58 Å
		ASN :87	Pi-Sigma	3,61 Å
			Pi-Donor	3,84 Å
		LEU :119	Pi-Amide	3,71 Å
P1- FP3	-7,3 Kcal/mol	LYS :43	C-H-bond	3,65 Å
		ASP :44	Pi-Alkyl	4,17 Å
		GLY :222	H-bond	2,23 Å
P2- FP3	-7,4 Kcal/mol	ASP :44	H-bond	2,67 Å
		ASP :44	H-bond	2,58 Å
		GLN :45	H-bond	2,29 Å
		ALA :46	H-bond	2,36 Å
		CYS :48	H-bond	3,04 Å
		TRP :215	H-bond	2,45 Å

Molecular docking results presented in the **Tables 10** and **11** include the value of binding affinity, the distances of bonds formed, and the interactions of ligands with amino acid residues. The comparison of results is done using chloroquine as a reference drug. Negative values indicate the smallest energy used by the receptor to interact with the ligand, so the interaction can take place spontaneously.⁵⁴ The lower the binding affinity value, the more stable the interaction between the ligand and the receptor. Based on the results obtained, it can be seen that all the compounds have different binding affinity values on each of the receptors. The binding affinity value on each receptor is negative. In the case of falcipain-2 (3BPF), it was found that the binding affinity value with chloroquine is low and equal to -5.2 Kcal/mol, while at the level of our compounds, P1 and P2 binding affinity values are lower and are respectively -6.7 Kcal/mol and -8.2 Kcal/mol with the same receptor. According to⁵⁵ active compounds are said to have the ability to interact with target receptors if they have a binding affinity value equal to or lower than that of the comparator drug.⁵⁶ For falcipain-3 (3BPM), chloroquine, which is also used as a comparison drug, has a binding affinity value of -5.6 Kcal/mol, whereas the compounds P1 and P2 have affinity values of -7.3 Kcal/mol and -7.4 Kcal/mol respectively. These results show that compounds P1 and P2 have an easier ability to interact with the 3BPM receptor than the reference drug. The low binding affinity values between our compounds and the receptors indicate the ease with which they interact with the receptor binding site.

3.4. Molecular Dynamic

The P2 product, which showed the best binding affinity to the *P. falciparum* FP-2 target protein, was chosen for an MD simulation study to assess its conformational stability and interaction over time. The protein-ligand complex resulting from the binding affinity prediction analysis was subjected to MD simulation using the original crystal structure of the target protein. The dynamic behavior of the bound P2-3BPF complex was assessed during a 50 ns.

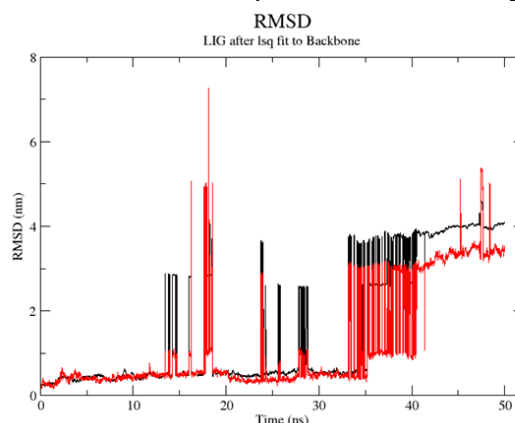


Fig. 19. RMSD plot for free 3BPF protein (Black) and 3BPF-P2 complex (Red); RMSD, root mean square deviation.

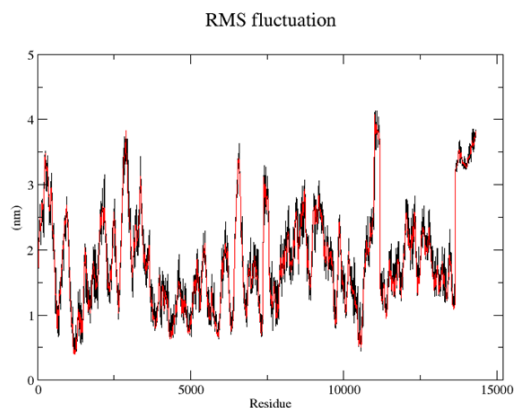


Fig. 20. RMSF plot of 3BPF-P2 complex and free protein; RMSF, root-mean-square fluctuations.

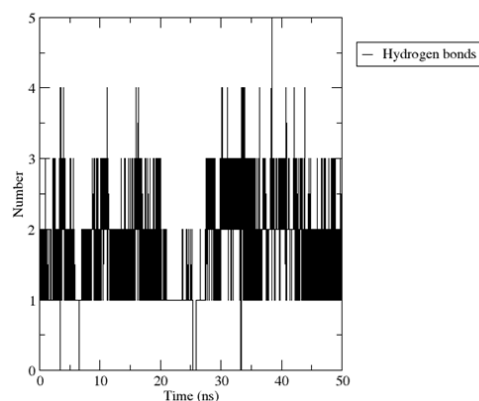


Fig. 21. Hydrogen bonds formed between 3BPF and compound P2.

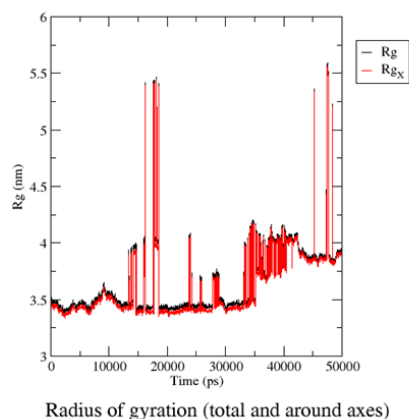


Fig. 22. Rg plot of free protein (Black) and 3BPF-P2 complex (Red); Rg, radius of gyration.

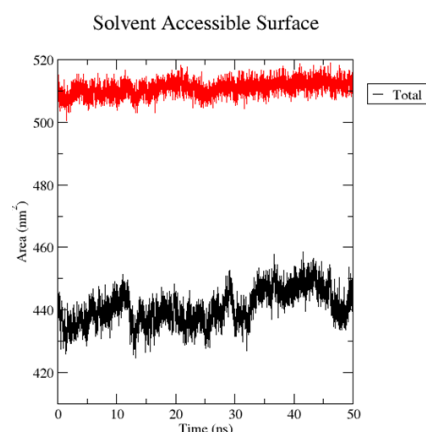


Fig. 23. SASA plot of 3BPF-P2 complex (red) and free protein (black); SASA, solvent-accessible surface.

The dynamic stability and behavior of the docked 3BPF-P2 complex were investigated using molecular dynamics simulation at 50 ns. Root mean square deviation (RMSD), root mean square fluctuation (RMSF), hydrogen bonding (HB), radius of gyration (Rg) and solvent accessible surface area (SASA) were calculated for the protein backbone. The RMSD results calculated for the complex showed good stability at the start of the simulation; from 14 ns onwards we witnessed a significant increase in RMSD values exceeding 2 nm suggesting a major conformational change. This structural transition could be linked to a deviation from the protein's initial conformation.⁵⁷

Given the critical role of each amino acid in ligand stability within the binding pocket, the RMSF value was calculated to explore residue flexibility (**Fig. 20**). The resulting RMSF values showed the presence of significant amino acid fluctuation observed at the binding site with fluctuation values ranging from 0.5 to 4 nm. High RMSF peaks were observed in the loop regions formed by the active site residues. The average RMSF fluctuation is around 1.5 nm. However, the marked increase in rmsf between suggests the presence of a dynamic event, potentially linked to a conformational change or interaction with the solvent.

The binding capacity of ligands is mainly determined by non-covalent interactions, such as hydrogen bonds, hydrophobic interactions and electrostatic interactions at the binding site. A high number of hydrogen bonds, as well as their stability over time, are key indicators of high binding affinity. According to (**Fig. 21**), a maximum of five hydrogen bonds were observed between compound P2 and protein 3BPF, two of which remained stable throughout the simulation, suggesting a robust and long-lasting interaction between ligand and protein.

The radius of gyration (Rg) diagram for the system studied is shown in **Fig. 22**. The average value of the radius of gyration of the complex was determined to be around 3.40 nm between 0 ns and 14 ns. This period is followed by a sudden increase to 5.5 nm. The high peaks observed indicate transient conformational changes linked to rearrangements at the protein level. The similarity between Rg and RgX suggests that conformational changes take place at the protein. These data confirm the RMSD results.

The solvent accessible surface area (SASA) of the protein and its complex was calculated during the simulation period and presented in **Fig. 23**. The results obtained reveal negligible variations in SASA values for the free protein and the complex. Indeed, SASA variation for both systems is almost stable.

3.5 ADMET Parameters

The ADMET prediction server used in this study is pkCSM,⁵⁸ a platform dedicated to the prediction and optimization of pharmacokinetic and toxicological properties of small molecules. This method is based on the use of graphical signatures to model molecular interactions. The results generated by pkCSM, evaluated on an external validation dataset, demonstrated an accuracy of 83.8% in the mutagenicity test,⁵⁹ confirming the robustness of this approach for assessing the risks associated with molecules. This study highlights the growing importance of computational approaches in drug design and development. The focus is on the analysis of the pharmacokinetic parameters of our two products from the reaction studied.

Table 12. ADMET: Prediction of Absorption and Distribution

Compounds	Absorption							Distribution			
	Wat. sol. (log mol/L)	Caco2 perm. (log Papp in 10 cm/s)	Intest. abso. (hum.) (%) Absorbed	Skin Per. (log Kp)	P-gP sub.	P-gP I inh.	P-gP II inh.	VDss (human) (log L/kg)	Frac. unbound (hum.) (Fu)	BBB perm. (log BB)	CNS perm. (log PS)
P1	-2.74	1.076	100	-2.735	Yes	No	No	-1.54	0.319	-0.795	-2.321
P2	-2.56	1.052	100	-2.735	Yes	No	No	-1.769	0.297	-0.808	-3.229

The results in **Table 12** show that our two compounds have good water solubility. The human intestinal absorption values are extremely high, indicating that our two compounds have a 100% chance of being absorbed by the human intestine. The Caco-2 cell line is generally used as an in vitro example of the human intestinal mucosa to calculate drug absorption by evaluating the logarithm of the apparent permeability coefficient (log Papp; log cm/s). A chemical compound is considered to have high Caco-2 permeability if its log Papp value is greater than 0.90 cm/s. Table 12 shows that our compounds have a high permeability, above 0.90 cm/s. The recommended value for skin permeability (log Kp), which is an important factor in improving drug efficacy and is particularly relevant in the creation of transdermal drug delivery, is greater than -2.5 cm/s.⁵⁸ The calculated log Kp values for the compounds are -2.735 cm/s. Therefore, these compounds are expected to have high skin penetration. The volume of distribution at steady state (VDss) and the blood-brain barrier (BBB) are two important factors to consider when assessing a drug's ability to disperse in the body. The higher the VDss, the more the drug is distributed in tissues rather than in plasma.⁵⁸ A chemical compound has a high VDss if its value is above 0.45 L/kg and a low VDss if its value is below -0.15 L/kg. The two products studied therefore have a low VDss. With regard to the blood-brain barrier, which determines a drug's ability to penetrate the brain while increasing its efficacy (fewer adverse effects), a molecule is able to rapidly cross the blood-brain barrier when log BB is greater than 0.3. Consequently, as the log BB values of all the derivatives examined are below 0.3, they are only marginally capable of crossing the blood-brain barrier.⁵⁹ The blood-brain surface permeability product (logPS) is a direct measure obtained from in situ cerebral perfusions with the compound directly injected into the carotid artery. According to Pires & al. work, compounds with a logPS greater than -2 are considered to penetrate the central nervous system, while compounds with a logPS greater than -3 are unable to penetrate the central nervous system (CNS). Our compounds are only weakly able to penetrate the central nervous system.

Table 13. ADMET properties: Metabolism and excretion

Compounds	Metabolism							Excretion	
	CYP2D6 subst.	CYP3A4 subst.	CYP1A2 inhibit	CYP2C19 inhibit.	CYP2C9 inhibit	CYP2D6 inhibit.	CYP3A4 inhibit	Total Clear. (log ml/min/kg)	Renal OCT2 subst.
P1	No	No	No	No	No	No	No	1.031	No
P2	No	No	No	No	No	No	No	1.023	No

Our results show that both compounds are not cytochrome P450 inhibitors, so are unlikely to be metabolized by P450. Excretion parameters obtained from pkCSM include total clearance and renal substrate OCT2. Both compounds, P1 and P2, have high total clearance values, suggesting that they can be rapidly excreted from the body. OCT2 is a protein transporter that plays an essential role in the absorption, elimination and renal clearance of drug compounds. Assessing the transfer of a candidate compound by OCT2 provides useful information concerning not only its clearance but also its potential contraindications.⁶⁰ The results show that P1 and P2 are not OCT2 substrates, so they will not remain in the body for long.

Table 14. ADMET properties: Toxicity

Compounds	Ames tox	Max. toler. dose (hum.) (log mg/kg/day)	Oral Rat Acu. Tox. (LD50 (mol/kg))	Oral Rat Chr. Tox. (LOAEL) (log mg/kg bw/day)	Hepat Toxic.	Skin Sens.

P1	No	0.704	2.008	1.744	No	No
P2	No	0.754	2.082	1.667	No	No

In the early stages of drug discovery, the compound identified as a potential candidate must display non-carcinogenic and non-hepatotoxic characteristics. The Ames test is a method used to assess the mutagenic potential of a compound using bacteria. According to our study, the compounds studied show a negative Ames test, so they are not mutagenic and will not act as carcinogens. The maximum recommended dose for our two products is over 0.477 log(mg/kg/day), which is considered a high dose. From our results, we can see that our products are neither hepatotoxic nor have skin toxicity. Another important element in determining the toxicity of a compound is the LD50 lethal dose, a test which determines the amount of a compound administered in a single dose that causes the death of 50% of a group of animals; LD50 values are high for P1 and P2, which is interesting.

4. Conclusion

In this theoretical study, we explored the intramolecular cyclization of benzastatin derivative, a molecule derived from *Streptomyces nitrosporeus*, using density functional theory (DFT) at the B3LYP/6-311G(d,p) level. Our study revealed that the quinoline-like product (P2) is both kinetically and thermodynamically favored over the indole-like product (P1), with the reaction pathway elucidated by detailed analysis of global and local reactivity indices, as well as electron localization function (ELF) calculations.

Molecular docking studies demonstrated that P1 and P2 have high binding affinities for the *Plasmodium falciparum* enzymes falcipain-2 (FP-2) and falcipain-3 (FP-3), key targets in the parasite's life cycle. Notably, the binding affinities of P1 and P2 were found to be higher than those of chloroquine, the reference antimalarial drug, suggesting their potential as potent inhibitors. Molecular dynamics (MD) simulations also demonstrated the stability of the P2-FP-2 complex up to 14 ns, on a 50 ns trajectory.

Pharmacokinetic and toxicity assessments carried out using the pkCSM platform indicated that both compounds possess favorable ADMET profiles, with good absorption, low toxicity and minimal risk of mutagenicity or hepatotoxicity. These properties, combined with their strong antimalarial potential, make P1 and P2 promising candidates for further development as new antimalarial agents.

In conclusion, this study provides valuable information on the reactivity, stability and pharmacological potential of benzastatin-derived compounds. The results underline the importance of computational methods in drug discovery, providing a solid basis for future experimental validation and the development of new therapeutic strategies against malaria. Compounds P1 and P2, in particular P2, may represent a significant advance in the search for effective antimalarial drugs, responding to the urgent need for new treatments in the face of growing drug resistance.

References

1. Rajput, A., Sharma, R., & Bharti, R. (2022). Pharmacological activities and toxicities of alkaloids on human health. *Mater. Today Phys.*, 48, 1407-1415.
2. Mvondo Mbala, E.-G., Mawete, D. T., Makiese, A. N., Kwiraviwe, P. L., Pangu, B. K., Nguimi, E. B., Kanyanga, R. C., Pieters, L., Degotte, G., Frederich, M., Matondo, A., Van Pelt, N., Caljon, G., Pirotte, B., Mavinga, B. M., & Bambi-Nyanguile, S.-M. (2024). Synthesis and pharmacological evaluation of fluoro/chloro-substituted acetyl and benzoyl esters of quinine as antimalarial agents. *Results Chem*, 7, 101284.
3. Dhameliya, T. M., Vekariya, D. D., Bhatt, P. R., Kachroo, T., Virani, K. D., Patel, K. R., Bhatt, S., & Dholakia, S. P. (2025). Synthetic account on indoles and their analogues as potential anti-plasmodial agents. *Mol. Divers.*, 29(1), 871-897.
4. Hariyanti, H., Mauludin, R., Sumirtapura, Y. C., & Kurniati, N. F. (2022). A review: Pharmacological activities of quinoline alkaloid of *Cinchona* sp. *Biointerface Res Appl Chem*, 13(4), 3.
5. Surur, A. S., Huluka, S. A., Mitku, M. L., & Asres, K. (2020). Indole: The after next scaffold of antiplasmodial agents? *Drug Des Devel Ther*, 14, 4855-4867.
6. Saxena, A., Majee, S., Ray, D., & Saha, B. (2024). Inhibition of cancer cells by quinoline-based compounds: A review with mechanistic insights. *Bioorg Med Chem*, 117681.
7. Gonçalves, B. M., Duarte, N., Ramalheite, C., Barbosa, F., Madureira, A. M., & Ferreira, M. J. U. (2024). Monoterpene indole alkaloids with anticancer activity from *Tabernaemontana* species. *Phytochem. Rev.*, 1-37.
8. Sulaiman, M., Jannat, K., Nissapatorn, V., Rahmatullah, M., Paul, A. K., de Lourdes Pereira, M., ... & Wiert, C. (2022). Antibacterial and antifungal alkaloids from Asian angiosperms: Distribution, mechanisms of action, structure-activity, and clinical potentials. *Antibiotics*, 11(9), 1146.

9. Masood, F., Khan, W., Khan, I., Khan, U., Majid, A., Khan, S. U., ... & Alam, M. M. (2024). Exploring the antibacterial and antibiofilm efficacy of *Psammogeton biternatum* Edgew and identification of a novel quinoline alkaloid using X-ray crystallography. *ACS Omega*, 9(43), 43557-43569.
10. Khan, N. A., Kaur, N., Owens, P., Thomas, O. P., & Boyd, A. (2022). Bis-indole alkaloids isolated from the sponge *Spongosorites calcicola* disrupt cell membranes of MRSA. *Int. J. Mol. Sci.*, 23(4), 1991.
11. Ouled Aitouna, A., Rossafi, B., El Alaoui El Abdallaoui, H., & Zeroual, A. (2025). Molecular electron density study on the [3+2] cycloaddition reaction between diphenylnitrilimine and cinnamaldehyde. *Sci. Rad*, 4 (1), 18-28.
12. Ti, H., Zhuang, Z., Yu, Q., & Wang, S. (2021). Progress of plant medicine-derived extracts and alkaloids on modulating viral infections and inflammation. *Drug Des Devel Ther*, 1385-1408.
13. Rasmussen, C., Alonso, P., & Ringwald, P. (2022). Current and emerging strategies to combat antimalarial resistance. *Rev. Anti-infect. Ther.*, 20(3), 353-372.
14. Amelo, W., & Makonnen, E. (2021). Efforts made to eliminate drug-resistant malaria and its challenges. *Biomed Res. Int.*, 2021(1), 5539544.
15. Raji, H., Zeroual, A., Chekroun, A., Mohammad-Salim, H., Syed, A., Elgorban, A. M., Abid, I., Verma, M., de Julián-Ortiz, J. V., & Benharref, A. (2024). Comprehensive study on the stereoselective epoxidation of aromatic atlantone: mechanism, ADME analysis, and potential as COVID-19 drug. *Chem. Heterocycl. Cmpd.* 60 (1), 568–574.
16. Ait Braim, I., Baammi, S., Ouled Aitouna, A., Zeroual, A., Chekroun, A., Mohammad-Salim, H., Al-Sadoon, M. K., Belghiti, M. E., de Julián-Ortiz, J. V., & Benharref, A. (2024). Quantum evaluation of novel epoxides: molecular docking, dynamics simulation, pharmacokinetics, stereoselectivity, and mechanistic insights into cis-himachalone and cis-himachalol epoxidation. *Chem. Heterocycl. Cmpd.* 60 (1), 575–583.
17. Lee, C., Yang, W., & Parr, R. G. (1988). Development of the Colle-Salvetti correlation-energy formula into a functional of the electron density. *Phys. Rev. B*, 37(2), 785.
18. Krishnan, R. B. J. S., Binkley, J. S., Seeger, R., & Pople, J. A. (1980). Self-consistent molecular orbital methods. XX. A basis set for correlated wave functions. *Chem. Phys.*, 72(1), 650-654.
19. Takano, Y., & Houk, K. N. (2005). Benchmarking the conductor-like polarizable continuum model (CPCM) for aqueous solvation free energies of neutral and ionic organic molecules. *J. Chem. Theory Comput.*, 1(1), 70-77.
20. Tomasi, J., & Persico, M. (1994). Molecular interactions in solution: An overview of methods based on continuous distributions of the solvent. *Chem. Rev.*, 94(7), 2027-2094.
21. Cancès, E., Mennucci, B., & Tomasi, J. (1997). A new integral equation formalism for the polarizable continuum model: Theoretical background and applications to isotropic and anisotropic dielectrics. *J. Chem. Phys.*, 107(8), 3032-3041.
22. Barone, V., & Cossi, M. (1998). Quantum calculation of molecular energies and energy gradients in solution by a conductor solvent model. *J. Phys. Chem. A*, 102(11), 1995-2001.
23. Cossi, M., Rega, N., Scalmani, G., & Barone, V. (2003). Energies, structures, and electronic properties of molecules in solution with the C-PCM solvation model. *J. Comput. Chem.*, 24(6), 669-681.
24. Domingo, L. R., Pérez, P., & Sáez, J. A. (2013). Understanding the local reactivity in polar organic reactions through electrophilic and nucleophilic Parr functions. *RSC Adv.*, 3(5), 1486-1494.
25. Domingo, L. R., Ríos-Gutiérrez, M., & Pérez, P. (2016). Applications of the conceptual density functional theory indices to organic chemistry reactivity. *Molecules*, 21(6), 748.
26. Lu, T., & Chen, F. (2012). Multiwfn: A multifunctional wavefunction analyzer. *Comput. Chem.*, 33(5), 580-592.
27. Lu, T., & Chen, Q. (2022). Multiwfn: A multifunctional wavefunction analyzer with enhanced features. *Comput. Chem.*, 43(8), 539-555.
28. Becke, A. D. (1993). Density-functional thermochemistry. III. The role of exact exchange. *The Journal of Chemical Physics*, 98(7), 5648-5652.
29. Becke, A. D. (1997). Density-functional thermochemistry. V. Systematic optimization of exchange–correlation functionals. *J. Chem. Phys.*, 107(20), 8554-8560.
30. Dunning Jr, T. H. (1989). Gaussian basis sets for use in correlated molecular calculations. I. The atoms boron through neon and hydrogen. *J. Chem. Phys.*, 90(2), 1007-1023.
31. Tomasi, J., Mennucci, B., & Cammi, R. (2005). Quantum mechanical continuum solvation models. *Chem. Rev.*, 105(8), 2999-3094.
32. Frisch, M. J., Trucks, G. W., Schlegel, H. B., Scuseria, G. E., Robb, M. A., Cheeseman, J. R., ... & Pople, J. A. (2009). *Gaussian 09, Revision A.02*. Gaussian, Inc., Wallingford, CT.
33. Frisch, M. J., et al. (2016). *Gaussian 16, Revision C.01*. Gaussian, Inc., Wallingford, CT.
34. McLean, A. D., & Chandler, G. S. (1980). Contracted Gaussian basis sets for molecular calculations. I. Second row atoms, Z=11–18. *J. Chem. Phys.*, 72(10), 5639-5648.
35. Zhao, Y., & Truhlar, D. G. (2008). The M06 suite of density functionals for main group thermochemistry, thermochemical kinetics, noncovalent interactions, excited states, and transition elements: two new functionals and systematic testing of four M06-class functionals and 12 other functionals. *Theor. Chem. Acc.*, 120(1-3), 215-241.
36. Abdoul-Hakim, M., Kenzy, C., Subramaniam, M., Zeroual, A., Syed, A., Bahkali, A. H., Verma, M., Wang, S., & Garmes, H. (2024). Elucidating chemoselectivity and unraveling the mechanism of 1,3-dipolar cycloaddition

- between diphenyl nitrilimine and (isoxazol-3-yl)methylbenzimidazole through molecular electron density theory. *Chem. Heterocycl. Compd.*, 60 (1), 617–626.
37. Perdew, J. P., Burke, K., & Ernzerhof, M. (1996). Generalized gradient approximation made simple. *Phys. Rev. Lett.*, 77(18), 3865.
 38. Grimme, S., Antony, J., Ehrlich, S., & Krieg, H. (2010). A consistent and accurate ab initio parametrization of density functional dispersion correction (DFT-D) for the 94 elements H-Pu. *J. Chem. Phys.*, 132(15), 154104.
 39. Grimme, S., Ehrlich, S., & Goerigk, L. (2011). Effect of the damping function in dispersion corrected density functional theory. *J. Comput. Chem.* 32(7), 1456-1465.
 40. Goerigk, L., & Grimme, S. (2011). A thorough benchmark of density functional methods for general main group thermochemistry, kinetics, and noncovalent interactions. *Phys. Chem. Chem. Phys.*, 13(14), 6670-6688.
 41. Keith, T. A. (2019). AIMAll (Version 19.10.12). TK Gristmill Software, Overland Park, KS, USA.
 42. Bader, R. F. W. (1990). *Atoms in Molecules: A Quantum Theory*. Clarendon Press, Oxford.
 43. Koch, W., & Holthausen, M. C. (2015). *A Chemist's Guide to Density Functional Theory*. John Wiley & Sons.
 44. Pearson, R. G. (1993). The principle of maximum hardness. *Acc. Chem. Res.*, 26(5), 250-255.
 45. Parr, R. G., & Pearson, R. G. (1983). Absolute hardness: companion parameter to absolute electronegativity. *J. Am. Chem. Soc.*, 105(26), 7512-7516.
 46. Pearson, R. G. (1997). Chemical hardness and density functional theory. *J. Chem. Sci.*, 109(6), 437-452.
 47. Fukui, K. (1982). The role of frontier orbitals in chemical reactions (Nobel Lecture). *Angewandte Chemie International Edition in English*, 21(11), 801-809.
 48. Chattaraj, P. K., & Maiti, B. (2003). HSAB principle applied to the time evolution of chemical reactions. *J. Phys. Chem. A*, 107(25), 4973-4975.
 49. Chattaraj, P. K., & Cedillo, A. (2007). Reactivity descriptors based on conceptual DFT. *Chem. Rev.*, 107(7), 2167-2199.
 50. Roy, R. K., & Ayers, P. W. (2008). On the correspondence between chemical hardness and electrophilicity indices. *J. Chem. Sci.*, 120(6), 819-825.
 51. Domingo, L. R. (2016). A new CDFT-based nucleophilicity index. *Molecules*, 21(10), 1319.
 52. Domingo, L. R., & Pérez, P. (2011). The nucleophilicity N index in organic chemistry. *Org Biomol Chem*, 9(20), 7168-7175.
 53. Kohn, W., & Sham, L. J. (1965). Self-consistent equations including exchange and correlation effects. *Phys. Rev.*, 140(4A), A1133.
 54. Levy, M. (1979). Universal variational functionals of electron densities, first-order density matrices, and natural spin-orbitals and solution of the v-representability problem. *Proc Natl Acad Sci*, 76(12), 6062-6065.
 55. Parr, R. G., & Yang, W. (1989). *Density Functional Theory of Atoms and Molecules*. Oxford University Press.
 56. Zhao, Y., & Truhlar, D. G. (2004). Hybrid meta density functional theory methods for thermochemistry, thermochemical kinetics, and noncovalent interactions: The MPW1B95 and MPWB1K models. *J. Phys. Chem. A.*, 108(4), 6908-6918.
 57. Dewar, M. J. S., Zoebisch, E. G., Healy, E. F., & Stewart, J. J. P. (1985). AM1: A new general purpose quantum mechanical molecular model. *J Am Chem Soc*, 107(13), 3902-3909.
 58. El Idrissi, K., Zeroual, A., & Garmes, H. (2025). Molecular docking against Covid-19 and HIV, and the role of catalysis in stereoselective cycloaddition reactions: A theoretical investigation of TiCl₄-promoted reactions between cyclopenta-1,3-diene and benzyl acrylate/benzyl 2-fluoroacrylate. *Curr. Chem. Lett.*, 14 (1), 279–288.
 59. Ryachi, K., Barhoumi, A., Atif, M., Zeroual, A., El Idrissi, M., & Tounsi, A. (2025). Advanced quantum and docking studies on the [3+2] cycloaddition of nitrile oxide with 1-Methyl-4-(Prop-1-en-2-yl)Cyclohex-1-ene: Exploring mechanisms and ADME properties. *Curr. Chem. Lett.*, 14 (1), 11–20.
 60. Barazzouq, A., Ouzebila, D., Hsissou, R., Daoudi, M., Bahkali, A. H., Zeroual, A., Wang, S., Syed, A., & El Idrissi, M. (2025). Theoretical anti-tuberculosis activity and molecular docking investigation of N-silylated heterocyclic compounds with benzyl chloride catalyzed by ammonium sulfate-doped red algae (AS@CRA). *Curr. Chem. Lett.*, 14 (1), 59–68.

